Andreev Modes from Phase Winding in a Full-Shell Nanowire-Based Transmon

A. Kringhøj,[1,2] G. W. Winkler,[3] T. W. Larsen,[1,2] D. Sabonis,[1,2] O. Erlandsson,[1,2]
P. Krogstrup,[1,4] B. van Heck,[5] K. D. Petersson,[1,2] and C. M. Marcus[1,2]

[1]*Center for Quantum Devices, Niels Bohr Institute, University of Copenhagen, 2100 Copenhagen, Denmark*
[2]*Microsoft Quantum Lab-Copenhagen, Niels Bohr Institute, University of Copenhagen, 2100 Copenhagen, Denmark*
[3]*Microsoft Quantum, Station Q, University of California, Santa Barbara, California 93106-6105, USA*
[4]*Microsoft Quantum Materials Lab-Copenhagen, 2800 Lyngby, Denmark*
[5]*Microsoft Quantum Lab Delft, Delft University of Technology, 2600 GA Delft, Netherlands*

(Received 23 August 2020; accepted 7 January 2021; published 29 January 2021)

We investigate transmon qubits made from semiconductor nanowires with a fully surrounding superconducting shell. In the regime of reentrant superconductivity associated with the destructive Little-Parks effect, numerous coherent transitions are observed in the first reentrant lobe, where the shell carries 2π winding of superconducting phase, and are absent in the zeroth lobe. As junction density was increased by gate voltage, qubit coherence was suppressed then lost in the first lobe. These observations and numerical simulations highlight the role of winding-induced Andreev states in the junction.

DOI: 10.1103/PhysRevLett.126.047701

In Josephson junctions formed by two superconductors separated by a coherent transmitting region, multiple electron-hole reflections at the superconductor boundaries result in a discrete subgap spectrum of Andreev bound states (ABSs) whose energy depends on the difference in phase, $\delta\varphi$, across the junction [1]. Recent microwave measurements have explored subgap Andreev spectra [2,3] and coherence [4,5], including effects of spin splitting and spin-orbit coupling in nanowire (NW) junctions [6,7].

Extending this development, hybrid semiconductor-superconductor NWs have been used to realize transmon-like qubits [8,9], operated at large ratios of the Josephson energy E_J to the charging energy E_C [10], where $\delta\varphi \sim 0$. The gate-tunable NW junctions used in these devices typically have a few channels with high transparency [11–13], which has observable consequences on qubit properties such as anharmonicity [13] and charge dispersion [14,15]. However, ABSs themselves are not readily observed in transmon measurements because near $\delta\varphi = 0$ transition frequencies are often much higher than the qubit frequency and well outside of the usual operational bandwidth (2–10 GHz). Tuning the phase difference near $\delta\varphi = \pi$ is usually required to lower ABS transitions to a measurable range [4,5]. However, this may not be the case when operating Josephson devices at finite magnetic fields, where ABS energies can be modulated by orbital effects in the semiconducting segments of NWs [16–19] and the Little-Parks effect in a NW with a fully enclosed superconducting shell [20–22]. Therefore, hybrid transmonlike qubit devices at finite magnetic fields can potentially reveal new information about the underlying Andreev processes, with implications on both junction and qubit parameters.

Here, we investigate low-energy ABSs in superconducting full-shell NW-based gatemons, which exhibit a destructive Little-Parks effect [20,23,24]. An applied magnetic field parallel to the NW induces a sequence of reentrant superconducting lobes, each associated with a different winding number, n, of the superconducting phase around the shell [21,22,25]. ABSs appear in the low-energy spectrum of the device in the first lobe ($n = 1$) and are absent in the zeroth lobe ($n = 0$), consistent with numerical simulations, also presented here.

Nanowire-based qubits in a circuit quantum electrodynamics [26,27] architecture were fabricated on high resistivity silicon substrates covered with a 20 nm thin NbTiN film [28]. Superconducting qubit islands, $\lambda/4$ distributed readout resonators with resonance frequencies $f_{\mathrm{res}} \sim 5$ GHz, transmission line, junction gates, and on-chip gate filters were defined with electron-beam lithography followed by reactive ion etching; see Fig. 1(a). NWs were placed on bottom-gates separated by a 15 nm thin HfO_2 dielectric. The NWs consisted of an InAs core of 140 nm in diameter, fully coated with 35 nm epitaxial Al [29]. By a selective wet etch, an ~400 nm segment of the Al shell was removed, creating a Josephson junction (JJ) [Fig. 1(b)]. Connecting superconducting leads to the ground and qubit island completed the gatemon circuit [8,9]. The ground plane was patterned with flux-pinning holes, crucial for magnetic field compatibility of the readout resonators [30,31]. Measurements are presented for two devices, denoted 1 and 2.

The qubit frequency f_{01} is measured as a function of magnetic field, B, applied parallel to the NW using both two-tone spectroscopy and single-tone spectroscopy. In two-tone spectroscopy, a pulsed qubit drive tone of variable

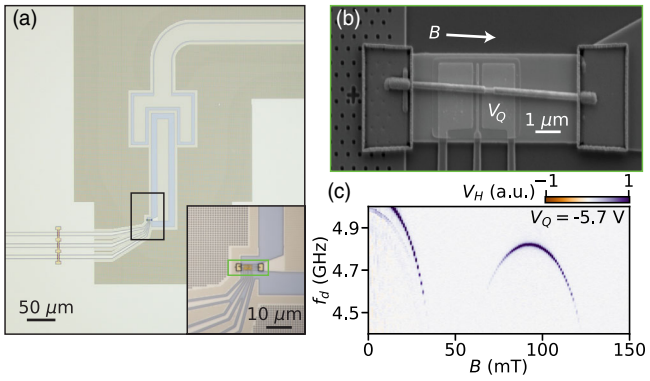

FIG. 1. (a) Optical micrograph of the qubit on ∼1 mm and ∼0.1 mm scale (inset) for device 1. The readout resonator is capacitively coupled to the rectangular qubit island, with an InAs/Al nanowire (NW) at the bottom (black rectangle). Flux-pinning holes are patterned near the island and resonator. (b) Electron micrograph of the NW [green rectangle in (a) inset], with junction controlled by gate voltage V_Q. Other electrodes not used. A magnetic field B is applied parallel to the NW. (c) Demodulated transmission voltage V_H as a function of B and qubit drive frequency f_d, showing reentrant qubit frequency f_{01} (device 1). Line median subtracted from each column.

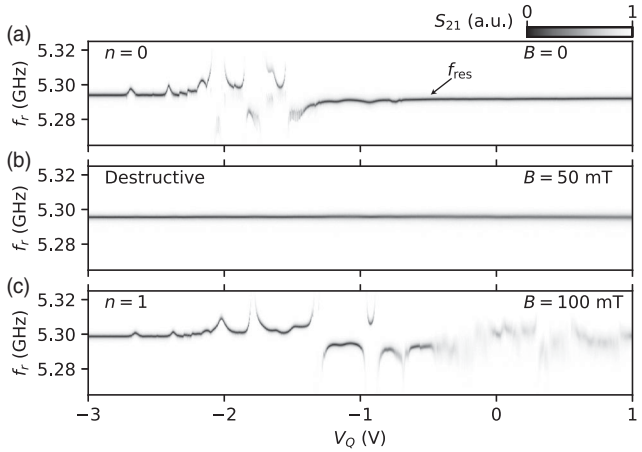

FIG. 2. Single-tone spectroscopy using transmission voltage amplitude S_{21} as a function of gate voltage V_Q and resonator drive frequency f_r in the zeroth lobe, destructive regime, and first lobe, for device 2. (a) In the zeroth lobe ($B = 0$, $n = 0$), the resonance frequency f_{res} (arrow) is modulated by V_Q due to the varying qubit frequency. (b) In the destructive regime ($B = 50$ mT), the resonator shows no dependence on V_Q. (c) In the first lobe ($B = 100$ mT, $n = 1$), the resonator shows gate dependence similar to (a) for $V_Q \lesssim -1$ V, and a broadened line, indicating increased damping, for $V_Q \gtrsim -1$ V.

frequency f_d is followed by a pulsed tone at a fixed readout frequency. By measuring the demodulated heterodyne transmission voltage V_H, the qubit frequency, f_{01}, can be inferred from the dispersive interaction between the qubit and resonator [26,27]. We measure both the in-phase (I) and quadrature (Q) components of the transmission signal, defining V_H by rotating the data in the IQ plane to maximize the signal along the real axis [32,33]. Two-tone measurement of the qubit frequency spectrum as a function of B [24], through the zeroth and first lobes ($n = 0$, 1) is shown in Fig. 1(c).

Single-tone spectroscopy directly measures the modulation of the resonance frequency f_{res} of the resonator due to its interaction with the qubit. Figure 2 shows the transmission voltage amplitude S_{21} as a function of the resonator drive frequency f_r. In the zeroth lobe ($B = 0$), we observe a nonmonotonic modulation of f_{res} associated with the voltage modulation of f_{01} as V_Q is increased from complete depletion at $V_Q \approx -3$ V [Fig. 2(a), $n = 0$]. For $V_Q \gtrsim -2$ V, several avoided crossings are observed, indicating that the qubit is tuned in and out of resonance with the resonator, as frequently observed for gatemon qubits [8,9]. For $V_Q \gtrsim -1$ V, f_{res} approaches its unshifted value, indicating a vanishing dispersive shift due to f_{01} being far above f_{res}. In the destructive regime [$B = 50$ mT, Fig. 2(b)], f_{res} shows no dependence on V_Q, as expected at flux $\Phi \sim \Phi_0/2$, where superconductivity in the Al shell is lost. In the first lobe [$B = 100$ mT, Fig. 2(c)], for $V_Q \lesssim -1$ V, f_{res} yields similar modulation compared to $n = 0$. This suggests a similar V_Q dependence of the qubit for $n = 1$. For $V_Q \gtrsim -1$ V, the spectrum is strikingly different from that measured in the zeroth lobe: the position of the resonant dip is subject to more fluctuations, and its width is increased.

We interpret the damping of the resonator as an increased decay rate caused by the qubit, indicating that the relaxation rate of the qubit is much larger than that of the resonator. We emphasize that the onset of enhanced relaxation in Fig. 2(c) is not gradual in B but occurs suddenly in the first lobe. This is demonstrated by a series of identical measurements taken at 5 mT intervals in both lobes [32], suggesting that the loss of qubit coherence for increasing V_Q is a phenomenon associated with $n = 1$, but not $n = 0$.

In the regime just before the onset of increased resonator relaxation, we directly map the qubit dependence of V_Q in the first lobe ($B = 100$ mT), by two-tone spectroscopy; see Fig. 3(a). Here, a range of unconventional energy transitions emerges. These transitions show strong gate dependence near certain values of V_Q, for instance around $V_Q = -2.88$ [dashed line, Fig. 3(a)], and several avoided crossings with the qubit transition, indicating that the transitions couple to the qubit. These transitions are observed for $n = 1$, clearly deviating from the spectra for $n = 0$ [32]. For $V_Q < -3.3$ V, only the usual gatemon transition frequencies (f_{01} and higher harmonics) are observed [32,34]. For $V_Q \gtrsim -2.7$ V qubit coherence is lost and the qubit frequency is not observed [32].

The unconventional transition frequencies are resolvable throughout the first lobe ($B \sim 70$–120 mT), while not being visible in the zeroth lobe for $B \lesssim 40$ mT, where only f_{01} and the multiphoton higher harmonics persist [Fig. 3(b)].

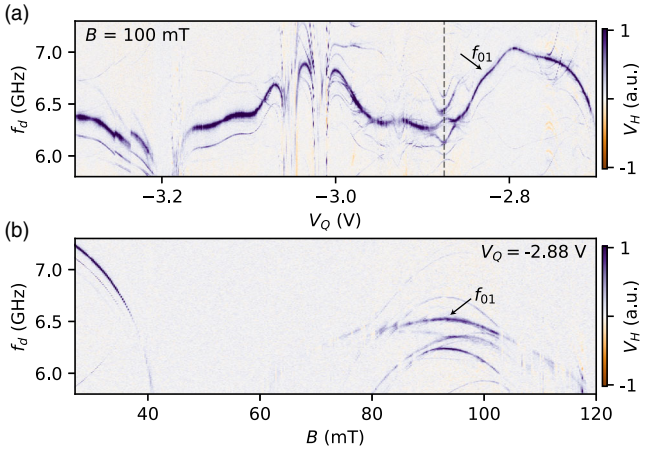

FIG. 3. (a) Two-tone spectroscopy shows demodulated transmission V_H as a function of gate voltage V_Q and qubit drive frequency f_d in the first lobe ($B = 100$ mT) for device 1. Near the main qubit transitions, which include f_{01} (arrow) and higher multiphoton harmonics (lines below f_{01} with the same V_Q dependence), numerous additional transitions are seen, with one example of their emergence and anticrossing with the qubit transition highlighted (dashed line). (b) V_H as a function of B and f_d at $V_Q = -2.88$ V [dashed line in (a)]. Qubit transition f_{01} (arrow) and additional transitions show reentrance from the destructive Little-Parks effect. In the zeroth lobe only the main qubit transitions are seen. f_{01} is associated with the broad transition [arrow in (a)] that persists in V_Q. We note a mirrored qubit transition peak for $V_Q \lesssim -3.1$ V and $V_Q \gtrsim -2.8$ V in (a) and for $B < 40$ mT in (b), associated with sideband leakage of the pulse modulation. Line median subtracted from each column.

This demonstrates that the emergence of these transitions is a distinct feature associated with $n = 1$, but not $n = 0$. These transitions both exhibit local maxima at larger values of B than f_{01}, and a distinctively different dependence on B, compared to f_{01} [arrow in Fig. 3(b)].

We associate the emergence of additional transitions and the loss of coherence with the increasing density of low-energy subgap states, which leads to a heavily damped qubit transition that in turn cause the damping of the readout resonator via the qubit-resonator coupling. The measurements in Figs. 2 and 3 are from two different devices with different threshold V_Q at which coherence is lost. The characteristic loss of coherence is the same in both devices.

Next, we perform simulations of a full-shell NW junction of similar dimensions as the measured devices. A hexagonal InAs/Al NW is modeled with the same methods and parameters as in Ref. [21], here adapted to the JJ geometry.

As shown in Ref. [21], the full-shell NW can host a topological or trivial phase for $n = 1$. Since the two phases cannot be distinguished purely from the excited ABS energies around $\delta\varphi = 0$, the presented results are obtained with parameters corresponding to the trivial phase for no spin-orbit coupling $\alpha = 0$, although the simulated ABS spectrum in the topological regime at finite α is qualitatively similar at $\delta\varphi \sim 0$ [32,35]. All simulations assume a band offset between InAs and Al of 140 meV. Figures 4(a) and 4(b) show longitudinal cuts of the simulated JJ with the electrostatic potential inside the InAs NW, which illustrate the formation of a depletion region for low back-gate voltages, occurring around $V_{\mathrm{BG}} = 0.38$ V, unlike an open junction at a representative $V_{\mathrm{BG}} = 0.71$ V. In the simulation, although V_{BG} is modeled as a global back gate, it is considered analog to the local bottom gate V_Q in the experiments.

To obtain a qualitative comparison with the experiment, we perform numerical simulations of the supercurrent using the Kwant package [37] and the analysis developed in Refs. [17,38]. From the critical current I_c, the simulated qubit frequency $f_{01}^{\mathrm{sim}} = \sqrt{8E_J E_C}/h = \sqrt{2E_C I_c/h\pi e}$ is obtained, where $E_C/h \sim 500$ MHz is estimated from electrostatic simulations of the qubit island [39] and $E_J = \hbar I_c/2e$. Figure 4(c) shows f_{01}^{sim} for $n = 0$ and $n = 1$ as a function of V_{BG}. While f_{01}^{sim} in the first lobe is reduced compared to the zeroth lobe, the general shapes are similar between the lobes. This is also observed experimentally; see Fig. 2. We interpret this reduction of f_{01}^{sim} as resulting from the overall reduced gap for $n = 1$, as discussed previously in Ref. [24].

By calculating the ABS transition energies from the density of states [32], the excitation frequencies f_A of energy states with two excited quasiparticles at $\delta\varphi = 0$ are identified and shown in Figs. 4(c) and 4(d) along with f_{01}^{sim}. When these transitions are near the qubit transition, they are expected to be activated in spectroscopic measurements via the coupling to the plasma mode [40] (coupling not included in our simulations). In the zeroth lobe all energies of two-quasiparticle states are well above the qubit frequency. However, in the first lobe these states are much lower in energy and f_A even cross the qubit frequency for several transitions for certain gate voltages as the junction is opened for increasing V_{BG}. This is in qualitative agreement with the experimental observations shown in Fig. 3(a).

Figure 4(d) shows the magnetic field dependence of f_{01}^{sim} and f_A for two different V_{BG}, representing a junction near depletion (top panel) and in an open regime (bottom panel). f_A for all two-quasiparticle transitions show a roughly parabolic dependence, distinctively different from f_{01}^{sim}. This is consistent with the expected scaling of two-quasiparticle state energies with Δ [41], whereas f_{01}^{sim} is expected to scale with $\sqrt{\Delta}$ (for $f_{01}^{\mathrm{sim}} = \sqrt{8E_J E_C}/h$ [10] and $E_J \propto \Delta$). These expectations are also consistent with the different field dependencies of the transitions, observed experimentally in Fig. 3(b). It is noted that the two-quasiparticle transitions for an open junction [Fig. 4(a), bottom] show additional kinks in the spectrum compared to a junction near depletion [Fig. 4(d), top]. We attribute this to the increasing density of Andreev transitions, which

results in crossing and close anticrossings of the ABSs. Furthermore, the local maxima of the simulated two-quasiparticle transitions are typically shifted to higher magnetic fields than the local maximum of f_{01}^{sim}, which is similar to the experimental observations shown in Fig. 3(b). This suggests that the wave functions of the associated states have a smaller effective cross section than the Al shell and thus are pierced by a correspondingly smaller flux.

The qualitative agreement between experiments and numerics suggests that the visible transition frequencies are explained by two-quasiparticle excitations of ABSs in the junction that emerge due to the nontrivial phase winding in the first lobe. When $n = 1$, the flux-induced winding causes a circumferential dependence of the phase of the order parameter on both sides of the junction. Therefore, ABSs can experience multiple phase differences depending on the particular trajectory they travel across the junction. In particular, for $n = 1$, trajectories traveling diagonally [dotted arrows in Fig. 4(b)] across the junction would experience a π-phase shift at $\delta\varphi = 0$. This is opposed to straight trajectories [solid arrow in Figs. 4(a) and 4(b)] that would not experience additional phase shifts. In general, for $n \neq 0$, the phase shift will depend on the specific start and end point of the trajectory, whereas for $n = 0$ the specific trajectory across the junction has no influence on the phase difference. Diagonal trajectories are more likely to occur as V_{BG} is increased and the potential barrier is reduced [Figs. 4(a) and 4(b)], which lowers the ABS energy at $\delta\varphi = 0$, resulting in an increasing density of low-energy states (see also Ref. [32]). We attribute the transitions near the qubit frequency, observed both experimentally (Fig. 3) and numerically (Fig. 4), to result from this increasing density of low-energy subgap ABSs for $n = 1$. Additionally, the emergence of these transitions immediately before the experimental observation of the increased relaxation of the resonator [Fig. 2(c)] suggests that the increased relaxation also occurs as a result of the increasing low-energy subgap density of states.

We focus on a narrow representative region of V_Q [Fig. 5(a)] to probe the coherence properties of the Andreev transitions in the first lobe. Throughout this regime the Andreev transitions can be driven coherently with examples of Rabi measurements across the transitions at $V_Q = -2.752$ V shown in Fig. 5(b). All transitions yield T_1-relaxation times of 3–5 μs, measured in a subsequent measurement. It is observed that the transitions closest to the uncoupled qubit transition yield the fastest oscillations at constant drive power [green and red panels in Fig. 5(b)]. We attribute this to be due to Andreev transitions

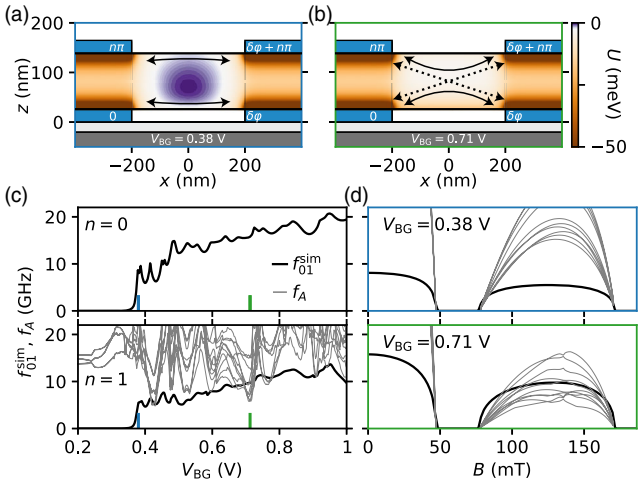

FIG. 4. Simulated electrostatic potential U near the InAs NW junction, between full-shell Al regions (blue) (a) for a nearly depleted junction, for voltage $V_{\mathrm{BG}} = 0.38$ V on the back-gate (gray) separated by HfO_2 dielectric (light gray) and (b) for a more populated junction, $V_{\mathrm{BG}} = 0.71$ V. For $V_{\mathrm{BG}} = 0.38$ V, the center region of the junction is depleted (purple). Superconducting phases are indicated in the shell regions. Diagonal (dotted arrows) and straight (solid arrows) trajectories across the junction are indicated. (c) Simulated qubit frequency f_{01}^{sim} (black) and two-quasiparticle transition frequencies f_A at $\delta\varphi = 0$ (gray) as a function of V_{BG} in the zeroth lobe ($B = 0$, $n = 0$, top panel) and in the first lobe (center of the lobe, $n = 1$, bottom panel). Two-quasiparticle transitions are off the scale shown for $n = 0$. (d) f_{01}^{sim} and f_A as a function of B for $V_{\mathrm{BG}} = 0.38$ V (top panel) and $V_{\mathrm{BG}} = 0.71$ V (bottom panel).

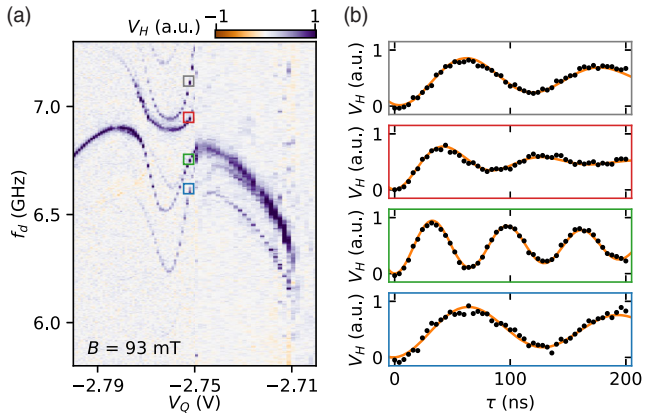

FIG. 5. (a) Demodulated transmission V_H as a function of B and qubit drive frequency f_d in a narrow range of V_Q in the first lobe ($B = 93$ mT) for device 1. The Andreev transitions are strongly gate dependent with local minima at similar V_Q. The drive power was increased by 10 dBm at $V_Q > -2.75$ V to ensure visibility of the qubit transition until coherence was lost for $V_Q \gtrsim -2.7$ V. Line median subtracted from each column. (b) Rabi measurements of V_H as a function of varying drive pulse width τ at $V_Q = -2.752$ V [colored squares in (a) match frame colors in (b)]. All transitions yield coherent Rabi oscillations, with the fastest oscillations of the transitions nearest the uncoupled qubit transition (green and red frames). The experimental data (black data points) are fitted to exponentially damped sinusoids (orange curves) and normalized to the extracted fit parameters.

being visible only indirectly through the coupling between the Andreev bound states and the qubit. This is expected as the coupling to the readout resonator in our setup is capacitive as opposed to an inductive coupling, which is generally required to directly probe Andreev states in a cQED-readout architecture [4,5]. The coupling depends on the detuning between the f_{01} and the Andreev transition frequency, and becomes stronger at smaller detuning. This results in the observed trend for the Rabi frequencies in Fig. 5(b), with larger Rabi frequencies at smaller detuning.

In conclusion, we demonstrate how the properties of a full-shell nanowire-based transmon qubit are modified via flux control, attributed to the phase winding induced by the Little-Parks effect. We show that the dispersive qubit readout is sensitive to the presence of unconventional Andreev transitions occurring at low frequencies in the Little-Parks regime. Future spectroscopy experiments based on an inductive coupling to the resonator may allow us to measure in detail the Andreev energy levels for different winding numbers, and potentially provide novel regimes of operation for Andreev qubits. Directly probing the Andreev spectrum may also allow experiments to investigate the predicted emergence of a topological phase [21], in particular for shorter junctions with a lower density of trivial Andreev bound states, as their presence complicates the distinction between topological and trivial phases.

We thank Andrey Antipov, Bela Bauer, Lucas Casparis, Anna Keselman, and Ivana Petkovic for valuable discussions. We acknowledge Marina Hesselberg, Karthik Jambunathan, Robert McNeil, Karolis Parfeniukas, Agnieszka Telecka, Shivendra Upadhyay, and Sachin Yadav for the device fabrication. Research was supported by Microsoft, the Danish National Research Foundation, and the European Research Council under Grant No. HEMs-DAM No. 716655.

[1] A. Andreev, J. Exp. Theor. Phys. **19**, 1228 (1964), http://www.jetp.ac.ru/cgi-bin/e/index/e/19/5/p1228?a=list.
[2] L. Bretheau, Ç. Ö. Girit, H. Pothier, D. Esteve, and C. Urbina, Nature (London) **499**, 312 (2013).
[3] D. J. van Woerkom, A. Proutski, B. van Heck, D. Bouman, J. I. Väyrynen, L. I. Glazman, P. Krogstrup, J. Nygård, L. P. Kouwenhoven, and A. Geresdi, Nat. Phys. **13**, 876 (2017).
[4] C. Janvier, L. Tosi, L. Bretheau, Ç. Ö. Girit, M. Stern, P. Bertet, P. Joyez, D. Vion, D. Esteve, M. F. Goffman, H. Pothier, and C. Urbina, Science **349**, 1199 (2015).
[5] M. Hays, G. de Lange, K. Serniak, D. J. van Woerkom, D. Bouman, P. Krogstrup, J. Nygård, A. Geresdi, and M. H. Devoret, Phys. Rev. Lett. **121**, 047001 (2018).
[6] L. Tosi, C. Metzger, M. F. Goffman, C. Urbina, H. Pothier, S. Park, A. L. Yeyati, J. Nygård, and P. Krogstrup, Phys. Rev. X **9**, 011010 (2019).
[7] M. Hays, V. Fatemi, K. Serniak, D. Bouman, S. Diamond, G. de Lange, P. Krogstrup, J. Nygård, A. Geresdi, and M. Devoret, Nat. Phys. **16**, 1103 (2020).
[8] T. W. Larsen, K. D. Petersson, F. Kuemmeth, T. S. Jespersen, P. Krogstrup, J. Nygard, and C. M. Marcus, Phys. Rev. Lett. **115**, 127001 (2015).
[9] G. de Lange, B. van Heck, A. Bruno, D. J. van Woerkom, A. Geresdi, S. R. Plissard, E. P. A. M. Bakkers, A. R. Akhmerov, and L. DiCarlo, Phys. Rev. Lett. **115**, 127002 (2015).
[10] J. Koch, T. M. Yu, J. M. Gambetta, A. A. Houck, D. I. Schuster, J. Majer, A. Blais, M. H. Devoret, S. M. Girvin, and R. J. Schoelkopf, Phys. Rev. A **76**, 042319 (2007).
[11] E. M. Spanton, M. T. Deng, S. Vaitiekėnas, P. Krogstrup, J. Nygård, C. M. Marcus, and K. A. Moler, Nat. Phys. **13**, 1177 (2017).
[12] M. F. Goffman, C. Urbina, H. Pothier, J. Nygård, C. M. Marcus, and P. Krogstrup, New J. Phys. **19**, 092002 (2017).
[13] A. Kringhøj, L. Casparis, M. Hell, T. W. Larsen, F. Kuemmeth, M. Leijnse, K. Flensberg, P. Krogstrup, J. Nygård, K. D. Petersson, and C. M. Marcus, Phys. Rev. B **97**, 060508(R) (2018).
[14] A. Bargerbos, W. Uilhoorn, C.-K. Yang, P. Krogstrup, L. P. Kouwenhoven, G. de Lange, B. van Heck, and A. Kou, Phys. Rev. Lett. **124**, 246802 (2020).
[15] A. Kringhøj, B. van Heck, T. W. Larsen, O. Erlandsson, D. Sabonis, P. Krogstrup, L. Casparis, K. D. Petersson, and C. M. Marcus, Phys. Rev. Lett. **124**, 246803 (2020).
[16] Ö. Gül, H. Y. Günel, H. Lüth, T. Rieger, T. Wenz, F. Haas, M. Lepsa, G. Panaitov, D. Grützmacher, and T. Schäpers, Nano Lett. **14**, 6269 (2014).
[17] K. Zuo, V. Mourik, D. B. Szombati, B. Nijholt, D. J. van Woerkom, A. Geresdi, J. Chen, V. P. Ostroukh, A. R. Akhmerov, S. R. Plissard, D. Car, E. P. A. M. Bakkers, D. I. Pikulin, L. P. Kouwenhoven, and S. M. Frolov, Phys. Rev. Lett. **119**, 187704 (2017).
[18] G. W. Winkler, D. Varjas, R. Skolasinski, A. A. Soluyanov, M. Troyer, and M. Wimmer, Phys. Rev. Lett. **119**, 037701 (2017).
[19] G. W. Winkler, A. E. Antipov, B. van Heck, A. A. Soluyanov, L. I. Glazman, M. Wimmer, and R. M. Lutchyn, Phys. Rev. B **99**, 245408 (2019).
[20] W. A. Little and R. D. Parks, Phys. Rev. Lett. **9**, 9 (1962).
[21] S. Vaitiekėnas, G. Winkler, B. van Heck, T. Karzig, M.-T. Deng, K. Flensberg, L. Glazman, C. Nayak, P. Krogstrup, R. Lutchyn, and C. Marcus, Science **367**, eaav3392 (2020).
[22] S. Vaitiekėnas, P. Krogstrup, and C. M. Marcus, Phys. Rev. B **101**, 060507 (2020).
[23] Y. Liu, Y. Zadorozhny, M. M. Rosario, B. Y. Rock, P. T. Carrigan, and H. Wang, Science **294**, 2332 (2001).
[24] D. Sabonis, O. Erlandsson, A. Kringhøj, B. van Heck, T. W. Larsen, I. Petkovic, P. Krogstrup, K. D. Petersson, and C. M. Marcus, Phys. Rev. Lett. **125**, 156804 (2020).
[25] Similar flux-dependent behavior may also be observed in semiconductor wires with a partial superconductor shell that have an electrostatic or materials configuration that prefers an accumulation layer around the outer edge of the wire [16,17,19].
[26] A. Wallraff, D. I. Schuster, A. Blais, L. Frunzio, R.-S. Huang, J. Majer, S. Kumar, S. M. Girvin, and R. J. Schoelkopf, Nature (London) **431**, 162 (2004).
[27] A. Blais, R.-S. Huang, A. Wallraff, S. M. Girvin, and R. J. Schoelkopf, Phys. Rev. A **69**, 062320 (2004).

[28] A. Kringhøj, T. W. Larsen, B. van Heck, D. Sabonis, O. Erlandsson, I. Petkovic, D. I. Pikulin, P. Krogstrup, K. D. Petersson, and C. M. Marcus, Phys. Rev. Lett. **124**, 056801 (2020).
[29] P. Krogstrup, N. L. B. Ziino, W. Chang, S. M. Albrecht, M. H. Madsen, E. Johnson, J. Nygård, C. M. Marcus, and T. S. Jespersen, Nat. Mater. **14**, 400 (2015).
[30] J. Kroll, W. Uilhoorn, K. van der Enden, D. de Jong, K. Watanabe, T. Taniguchi, S. Goswami, M. Cassidy, and L. Kouwenhoven, Nat. Commun. **9**, 4615 (2018).
[31] J. Kroll, F. Borsoi, K. van der Enden, W. Uilhoorn, D. de Jong, M. Quintero-Pérez, D. van Woerkom, A. Bruno, S. Plissard, D. Car, E. Bakkers, M. Cassidy, and L. Kouwenhoven, Phys. Rev. Applied **11**, 064053 (2019).
[32] See Supplemental Material at http://link.aps.org/supplemental/10.1103/PhysRevLett.126.047701 for additional details on the experimental setup, field dependence of resonator frequency, gate dependence in zeroth and first lobe, and details of the numerical simulations.
[33] See accompanying analysis code for details on data analysis and theoretical simulations at https://doi.org/10.5281/zenodo.3988547.
[34] We note the transitions at $V_Q \sim -2.75$ V in Fig. 3(a) with opposite curvatures compared to the majority of the transitions observed. These transitions are also visible in the zeroth lobe [32]. We speculate that these transitions arise from excited Andreev states, making them visible at low frequencies for $n = 0$ also.
[35] The topological regime would manifest itself via a splitting of the qubit plasma frequency due to the coherent single-electron tunneling mediated by a Majorana coupling [36], but this signature was not observed in these devices [24].
[36] E. Ginossar and E. Grosfeld, Nat. Commun. **5**, 4772 (2014).
[37] C. W. Groth, M. Wimmer, A. R. Akhmerov, and X. Waintal, New J. Phys. **16**, 063065 (2014), the code is publicly available at https://kwant-project.org/.
[38] V. P. Ostroukh, B. Baxevanis, A. R. Akhmerov, and C. W. J. Beenakker, Phys. Rev. B **94**, 094514 (2016).
[39] COMSOL, Inc., www.comsol.com.
[40] A. Keselman, C. Murthy, B. van Heck, and B. Bauer, SciPost Phys. **7**, 50 (2019).
[41] C. W. J. Beenakker, Phys. Rev. Lett. **67**, 3836 (1991).